

Building of rich (111) grain boundary in copper for syngas in electrochemical CO₂ reduction

Xia Bai ^{a,1}, Jingmin Ge ^{b,1}, Huanhuan Yang ^{a,*}, Huiwen Tian ^a, Xueqi Liu ^a, Shiying Li ^c, Zhikun Peng ^a, Yaxi Li ^a, Jiahao Wang ^d, Hongpo Liu ^{a,*}, Qun Xu ^{a,*}

^a Henan Institute of Advanced Technology, Zhengzhou University, Zhengzhou 450002, China

^b School of Mechanics and Safety Engineering, Zhengzhou University, Zhengzhou 450001, China

^c State Key Laboratory of Coal Conversion, Institute of Coal Chemistry, Chinese Academy of Sciences, Taiyuan 030001, China

^d School of Chemistry and Materials Science, Anhui Normal University, Wuhu 241002, China



ARTICLE INFO

Keywords:

Cu(111) grain boundary
Electrochemical CO₂ reduction
Reconstruction
Syngas

ABSTRACT

Building of grain boundary (GB) in Cu-based catalysts has been demonstrated to be an efficient strategy to control the product selectivity of electrochemical CO₂ reduction reaction (eCO₂RR). However, the fabrication and modulation of GBs in Cu are still challenging. In this study, a series of bare Cu catalysts with controllable density of Cu(111) GBs were investigated systematically for eCO₂RR. These catalysts exhibit superior eCO₂RR performance for syngas production with a high FE of ~80 % and tunable H₂/CO ratio of 0.46–2.78. Three-dimensional wormlike Cu with abundant (111) GBs displays a stable H₂/CO ratio of ~0.5 over a wide potential range from -0.9 to -1.2 V (vs. RHE). In situ Raman and ATR-SEIRAS spectroscopy combined with DFT calculations reveal that Cu(111) GBs enhance the adsorption of CO₂, lower the energy barriers of CO₂ to *COOH and *CO, further highlighting the potential to control syngas production with desirable proportion over Cu-based catalysts.

1. Introduction

Accumulation of CO₂ in the atmosphere leads to serious environmental problems, such as global warming, ocean acidification and so on [1,2]. The effective utilization and conversion of CO₂ have become urgent. Electrochemical CO₂ reduction reaction (eCO₂RR), which can use intermittent electricity produced via renewable energy and convert CO₂ to value-added products, is one of the most promising approaches [3–12]. Syngas with tunable H₂/CO ratio is potential feedstock for downstream chemicals production, *e.g.*, Fischer-Tropsch reaction and methanol synthesis [13–19]. In recent years, precious metals or their composites such as porous Au, Cu/Au core-shell arrays, and Pd/Cu core/shell icosahedra have been reported to catalyze the eCO₂RR for production of syngas [20–22]. But, the use of noble metal is a limitation due to the high cost and insufficient resource. Importantly, these reported catalysts gave low FE_{COmax} of less than 40 %, resulting in the absence of H₂/CO ratio < 1. Compared to usual noble metal catalysts, Cu-based materials have attracted broad research interest in the process of eCO₂RR due to its natural abundance. However, the high C=O

dissociation energy (750 kJ/mol) of CO₂ and moderate intermediate adsorption energy of Cu lead to poor CO selectivity and limited H₂/CO ratio [20,23]. One of the reported alternative strategies aimed at tuning the eCO₂RR-to-syngas performance of bare Cu is modifying it with a foreign component [24]. Obviously, this might complicate the catalytic system, and the contributions of introduced foreign component and Cu species to the eCO₂RR performance might be mingled together so that a clear mechanistic understanding becomes difficult. Therefore, the preparation of bare Cu nanostructured catalysts for eCO₂RR-to-syngas is highly desirable.

Grain boundaries (GBs) in metals are regarded as effective sites to improve the catalytic properties [25,26]. Theoretical calculations suggested that GBs induce strained regions in polycrystalline materials, which may break local spatial symmetry around GBs and influence the binding energy of reaction intermediate, resulting in enhanced reaction rate of CO₂-to-CO [27]. Recently, a GBs-rich Cu catalyst was fabricated by the additive-control electrodeposition, in which poly(vinylpyrrolidone) was used as an additive. It was noticeable that the poly(vinylpyrrolidone) molecule was indispensable to introduce GBs into Cu

* Corresponding authors.

E-mail addresses: yanghh@zzu.edu.cn (H. Yang), hongpoliu@zzu.edu.cn (H. Liu), qunxu@zzu.edu.cn (Q. Xu).

¹ These authors contributed equally.

nanoparticles [25]. Another reported method for fabrication of Cu GBs like e-beam evaporation needed specific instrument of e-beam evaporator and vacuum system [28]. Obviously, the acquired GB-rich Cu is inevitably contaminated by polymeric additives and is usually sensitive to the synthesis conditions.

Oxide crystals in heat-quench Cu electrode were fragmented into nano-sized irregular Cu grains under negative potentials, resulting in an intricate network of GBs [27]. However, this fragmentation process also exposed a large number of various high-index facets. Similar dynamic

restructuring has also been found in CuO nanosheet with formation of abundant Cu(100)/Cu(111) GBs [29]. Synergism between the GBs and facets or morphological structure for C–C coupling was emphasized in these reports rather than for CO formation [28,30,31]. In addition, Kanan's group [32] proposed that GBs that bind CO more strongly than terrace and step sites account for the selective reduction of CO to multi-carbon oxygenates in KOH. But it is unclear whether these GBs are also active to produce CO from eCO₂RR in bicarbonate electrolytes. CO is typically considered to be the key intermediate toward the formation

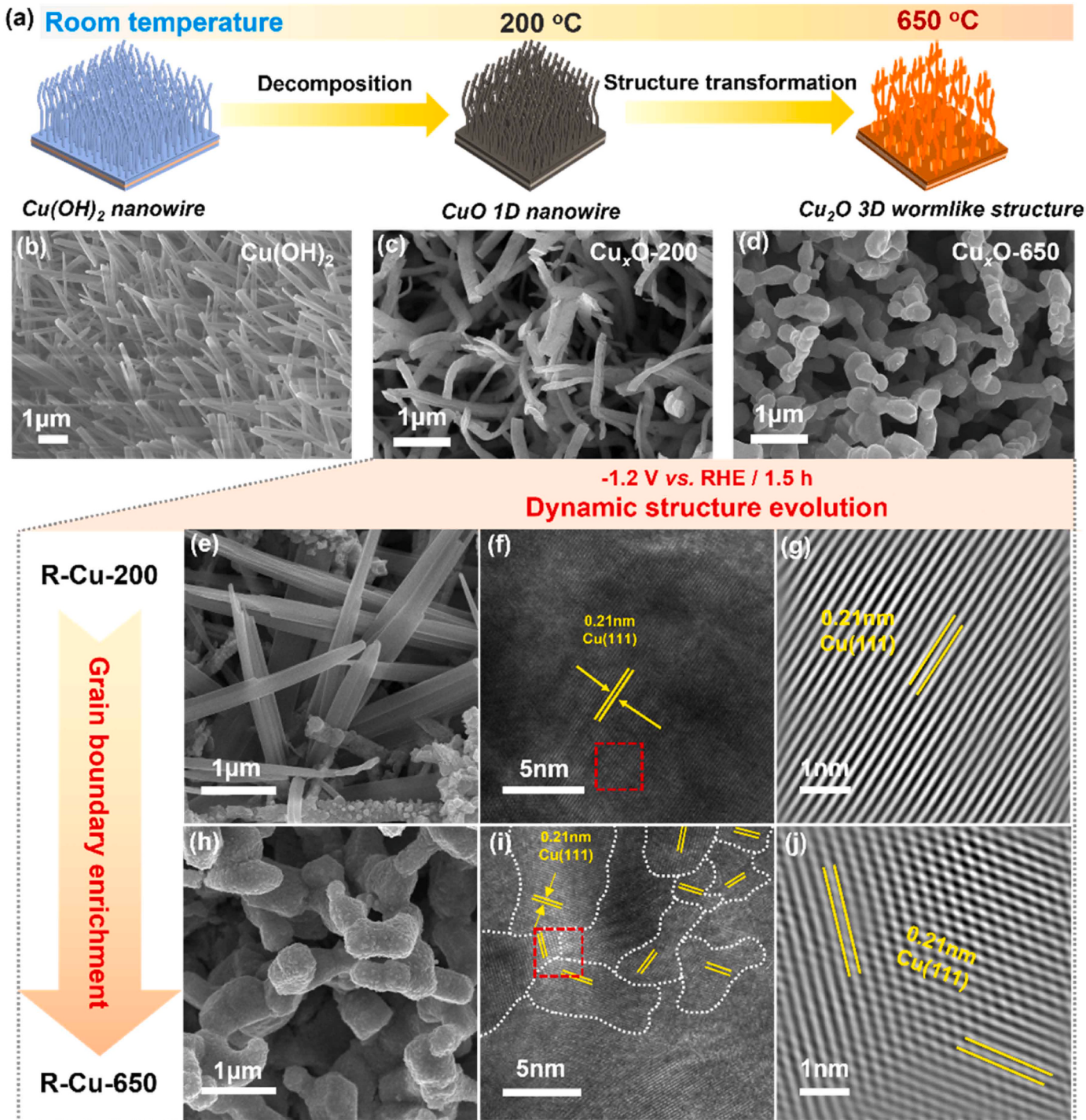


Fig. 1. (a) Schematic illustration of the preparation procedure of Cu_xO-T; (b) SEM images of (b) Cu(OH)₂ nanowires precursor on Cu foam, (c) Cu_xO-200 and (d) Cu_xO-650; (e) SEM image and (f) HRTEM image of R-Cu-200; (g) Inverse Fast Fourier Transformation (FFT) image of selected area in (f); (h) SEM image and (i) HRTEM image of R-Cu-650; (j) Inverse FFT image of selected area in (i).

of multi-carbon products in eCO₂RR, and also is a desirable product for the generation of syngas [33]. Therefore, it is of great interest to clarify the role of GBs in reduction of CO₂ to CO, and efficient approaches to controllably fabricate GBs with different density in Cu are of significance.

Herein, bare Cu catalysts with different density of (111) GBs were prepared by the temperature-control annealing and subsequently electrochemical pre-reduction (Fig. 1) for systematical investigation of eCO₂RR-to-syngas. The as-prepared catalysts show a decent eCO₂RR-to-syngas performance with a widely tunable H₂/CO ratio of 0.46–2.78. In addition, a syngas FE of ~80 % and a stable H₂/CO ratio of around 0.5 over a large potential range (−0.9 to −1.2 V vs. RHE) were achieved. The activity of eCO₂RR to CO increased with the density of Cu(111) GBs. For the first time, it is found out that building three-dimensional (3D) wormlike structure with higher density of Cu(111) GBs facilitates the adsorption of CO₂, lowers the energy barriers of CO₂ to *COOH intermediate and further to *CO.

2. Experimental section

2.1. Chemicals

Sodium hydroxide (NaOH, ≥ 98.0 %) and potassium hydroxide (KOH, 95.0 %) were purchased from Aladdin. Ammonium persulfate ((NH₄)₂S₂O₈, AR grade, ≥ 98.0 %) and absolute ethanol (AR grade, ≥ 99.7 %) were purchased from Sinopharm Chemical Reagent Co., Ltd. (Shanghai, China). Potassium hydrogen carbonate (KHCO₃, AR grade, 99.5 %) was purchased from Macklin. Hydrochloric acid (HCl, AR grade, 36.0 ~ 38.0 %) and acetone (AR grade, ≥ 99.5 %) were purchased from XILONG SCIENTIFIC Co., Ltd. (Guangdong, China). Ar (≥ 99.999 %) and CO₂ (≥ 99.999 %) were provided by Henan Yuanzheng Special Gas Co., Ltd. All chemicals were used as received without further treatment. Deionized water (18 MΩ·cm) was prepared with an ultra-pure purification system.

2.2. Synthesis of Cu(OH)₂ nanowire

The Cu(OH)₂ nanowire was in situ fabricated on Cu foam according to the procedures shown in Fig. S1[34,35]. Briefly, commercial Cu foam was ultrasonic cleaned with ethanol, 0.1 M HCl, acetone and deionized water in sequence. The cleaned Cu foam was immediately placed vertically in an aqueous solution of 2.667 M NaOH and 0.133 M (NH₄)₂S₂O₈ for 20 min. The formed Cu(OH)₂ nanowire on Cu foam was washed with deionized water and ethanol for three times, respectively, and then dried under vacuum at 60 °C overnight.

2.3. Synthesis of Cu_xO-T and R-Cu-T

The obtained Cu(OH)₂ nanowire was calcined in Ar at designed temperature of 200, 350, 500, 650 or 800 °C for 4 h in a tube furnace. The resulted samples were designated as Cu_xO-T (T represents the calcined temperature). Cu_xO-T was then pre-reduced at −1.2 V (vs. RHE) for 1.5 h to obtain R-Cu-T.

2.4. Electrochemical measurements

Electrocatalysis reduction of CO₂ (recorded on a CHI 660E electrochemical workstation) was performed in a three-electrode system with a gas-tight H-type electrolyzer. The cathodic compartment and the anodic compartment were separated by a Nafion 117 membrane. A platinum sheet electrode (1 × 1 cm²) and a leak-free KCl-saturated Ag/AgCl electrode were used as counter electrode and reference electrode, respectively. In situ generated freestanding Cu_xO-T on Cu foam or polished Cu foam (1 × 1 × 2 cm²) was directly used as a working electrode. All potentials measured against Ag/AgCl reference electrode in this work were converted to the reversible hydrogen electrode (RHE)

according to the Nernst formula:

$$E \text{ (vs. RHE)} = E \text{ (vs. Ag/AgCl)} + 0.197 \text{ V} + 0.0591 \text{ V} \times \text{pH} \quad (1)$$

Before the reaction, CO₂ was continuously purged into the 0.1 M KHCO₃ electrolyte for at least 30 min until saturation (pH = 6.8). This is followed by the pre-reduction of working electrode at −1.2 V (vs. RHE) for 1.5 h to obtain R-Cu foam or R-Cu-T. During the reaction, CO₂ was delivered into the cathodic compartment at a flow rate of 20 mL/min. The gaseous products were on-line analyzed by a gas chromatograph (Haixin Chromatography, Shanghai), which was equipped with a thermal conductivity detector (TCD) for analysis of H₂ and a flame ionization detector (FID) for analysis of CO and hydrocarbons. The liquid products were analyzed by ¹H nuclear magnetic resonance (NMR) spectroscopy on a Bruker 400 MHz NMR spectrometer. 490 μL of the collected electrolyte (containing CO₂ reduction products) was mixed with 100 μL of D₂O, and 10 μL of 0.15 vol% DMSO (in 0.1 M KHCO₃) was added as an internal standard. The Faradaic efficiency (FE) of specific product was calculated via the equations as follows:

$$\text{gas products: FE (\%)} = nFC_i\nu P/jRT \quad (2)$$

$$\text{liquid products: FE (\%)} = nFC_iV/Q \quad (3)$$

where *n* is the transferred electron numbers to generate target product; *F* is the Faradaic constant (96,485.33 C/mol); *C_i* is the volume concentration of gas product *i* (ppm, × 10^{−6}) or molar concentration of liquid product *i* (mol/L); *ν* is the flow rate of CO₂ (m³/s); *P* is the standard atmospheric pressure (1.013 × 10⁵ Pa); *R* is the ideal gas constant (8.314 J/mol/K); *T* is the room temperature (298.15 K); *j* is the total current (A) and *Q* is the total charge (C) during the eCO₂RR.

For experiments in flow cell (GaossUnion, 101017-1.2), 5 mg of the catalyst separated from the Cu foam was scattered in 980 μL of absolute ethanol and 20 μL Nafion by ultrasound, and controllably dropped onto the carbon paper (0.5 × 2 cm, SGL-28BC) to acquire gas diffusion electrode (GDE) with a loading mass of about 1 mg·cm^{−2}. The prepared GDE was placed between the catholyte and gas chambers with the catalyst side faced with the catholyte chamber, in which the catholyte and anolyte chambers were separated by an anion-exchange membrane (AEM, FAB-PK-130, Fumasep). The eCO₂RR performance of R-Cu-500 was investigated on a CHI 760E electrochemical workstation equipped with a current amplifier (CHI 680 C) at room temperature. A platinum sheet electrode (0.5 × 2 cm) and Ag/AgCl electrode were used as the counter and reference electrodes, respectively. 1.0 M of KOH electrolyte was fed into the cathode and anode chambers via peristaltic pumps (NKCP-B04B, Spurlin Co., Ltd.) with a flow rate of 15 rpm, while CO₂ gas with a flow rate of 100 mL min^{−1} was fed into the gas chamber [36].

The linear sweep voltammetry (LSV) was conducted at a range from −0.2 to −1.2 V (vs. RHE) with a scan rate of 0.01 V/s in CO₂- or Ar-saturated electrolyte. Electrochemical active surface area (ECSA) was calculated in accordance with the following function:

$$\text{ECSA} = R_f \times S \quad (4)$$

$$R_f = C_{dl(Cu_xO-n)} / C_{dl(Cu \text{ foam})} \quad (5)$$

where *R_f* is the roughness factor and *S* is the geometrical surface area of the working electrode. *C_{dl}* is the double-layer capacitance, which was obtained from the cyclic voltammetry (CV) test with a scan rate of 2, 4, 6, 8 and 10 mV/s at the non-Faradaic area (−0.0918 to 0.0082 V vs. RHE) in Ar-saturated 0.1 M KHCO₃. $\Delta j/2$ (i.e., $(j_a - j_c)/2$) was plotted against the scan rate and the slope was the *C_{dl}*. *j_a* and *j_c* are anodic and cathodic current density normalized by the geometric area of the electrode, respectively. Nyquist plot of electrochemical impedance spectroscopy (EIS) was tested in the frequencies ranging from 10^{−2} to 10⁶ Hz at open circuit potential (OCP) with amplitude of 5 mV.

2.5. Characterizations

X-ray diffraction (XRD) patterns were obtained on an X-ray diffractometer (Rigaku Ultima IV) with Cu K α radiation ($\lambda = 1.5418 \text{ \AA}$) operated at 40 KV and 40 mA. The morphology and microstructure of the samples were characterized by scanning electron microscope (SEM, ZEISS Sigma 300) with an accelerating voltage of 0.02–30 KV, and (high-resolution) transmission electron spectroscopy ((HR)TEM, FEI/Talos F200S) with total beam current of $> 150 \text{ nA}$. X-ray photoelectron spectroscopy (XPS, Thermo Scientific K-Alpha) and X-ray induced Auger electron spectroscopy (XAES) were performed to distinguish the valence state of the element. Raman spectra were recorded on a confocal Raman microscope (HORIBA FRANCE SAS, LabRAM Soleil nano). Temperature-programmed desorption of CO₂ (CO₂-TPD) was carried out on an AutoChem II 2920 Chemisorption Analyzer. 100 mg sample was treated at 180 °C for 30 min in Ar (30 mL/min). This is followed by lowering down the temperature to 50 °C and adsorbing CO₂ for 1 h from 10 % CO₂/Ar (30 mL/min). After that, the sample was purged with an Ar flow (30 mL/min) for 30 min to remove physisorbed CO₂. Finally, the sample was heated from 50 to 600 °C at a rate of 10 °C/min, and the desorbed CO₂ was monitored by a thermal conductivity detector.

All obtained R-Cu-T and the ones after long-term tests (R-Cu-T-used) were rinsed with deionized water and then immediately immersed into liquid nitrogen after being removed from the electrochemical system. The samples were vacuum dried at 45 °C for 12 h and vacuum stored until the measurements.

In situ Raman spectra were carried out on a confocal Raman spectrometer (HORIBA FRANCE SAS, LabRAM Soleil nano) equipped with a 50× objective lens and a 638 nm excitation laser of 30 mW. The measurements were conducted with a tailored H-type flow cell (GaossUnion, C031) by pumping CO₂-saturated 0.1 M KHCO₃ (8 mL/min) as electrolyte. Cu_xO-T was used as working electrode directly. The Raman spectra were collected along with time at -1.2 V (vs. RHE). Each spectrum was recorded with a 20 s collection.

In situ attenuated total reflection surface-enhanced infrared absorption spectroscopy (ATR-SEIRAS) was measured by an INVENIO R FT-IR spectrometer equipped with a liquid nitrogen cooled mercury cadmium telluride (MCT) detector. The spectro-electrochemical cell furnished with a SPEC-I ATR (Shanghai Yuanfang Technology CO., Ltd.) was filled with 0.1 M KHCO₃. The working electrode was made by depositing the catalyst ink on Au-plated silicon prism [37], so that the IR beam can probe the intermediate species produced during eCO₂RR. Ag/AgCl electrode and graphite rod electrode were used as reference electrode and counter electrode, respectively. During the test, CO₂ was kept bubbling into the electrolyte with a flow rate of 20 mL·min⁻¹. Experiments were performed at different applied potentials from -0.4 to -1.2 V (vs. RHE). The spectrum was collected at OCP with CO₂-saturated 0.1 M KHCO₃ as a reference. All spectra were collected at a resolution of 8 cm⁻¹ in absorbance mode.

2.6. Calculated model and methods

The density functional theory (DFT) calculations were carried out on Vienna Ab-initio Simulation Program (VASP). The method of Perdew-Burke-Ernzerhof (PBE) generalized gradient approximation (GGA) was adopted, and the cutoff energy of the plane wave basis was set to 400 eV. The convergence threshold for energy and the k-point separation were 10⁻⁵ eV and 0.01 Å⁻¹, respectively.

To calculate the adsorption energy (ΔE) of the intermediate, the equation was used:

$$\Delta E = E_{\text{substrate+adsorbate}} - E_{\text{substrate}} - E_{\text{adsorbate}} \quad (6)$$

Where E is the energy of the system.

The Gibbs free energies were calculated at 298 K and 1 atm by the equation:

$$G = E_{\text{DFT}} + ZPE - TS + \int C_v dT \quad (7)$$

Where E_{DFT} is the electronic structure energy, ZPE is the zero-point vibrational energy, T is the temperature, and S is the entropy. $\int C_v dT$ is the heat capacity. The value of ZPE, TS and $\int C_v dT$ were adopted from the method of Peterson et al. [38].

3. Results and discussion

Fig. 1a,b and **S1** show that Cu(OH)₂ nanowires precursor was first in situ grown on the smooth surface of Cu foam. Cu_xO-T with different morphology were obtained after the as-prepared Cu(OH)₂ nanowires were annealed in Ar at different temperatures (**Fig. 1a,c,d** and **S2**). The Cu_xO-T on Cu foam was then pre-reduced at -1.2 V (vs. RHE) for 1.5 h (**Fig. S3**), resulting in dark red R-Cu-T. As shown in SEM images (**Fig. 1e**, **h** and **S4**), the surface of all R-Cu-T was rough and abundant nanometer-sized particles were observed. This indicates the dynamic reconstruction of Cu_xO-T at the pre-reduction stage. Specifically, the reconstruction of Cu_xO-200 was not complete and some surface of the nanowires was still smooth (**Fig. 1e**). Although the reconstruction was complete, pre-reduced Cu_xO-350 contains both small Cu particles with sub-nanometer size and large Cu particles with average size of 180 nm (**Fig. S4a,b**). While for Cu_xO-500 and Cu_xO-650, the surface reconstruction was complete and the large polyhedron particles were transformed into fragmented ones with uniform size after pre-reduction (**Fig. 1h** and **S4e,f**). HRTEM images reveal that the R-Cu-200 shows some uniform lattice orientation without GBs (**Fig. 1f,g**), while R-Cu-500 and R-Cu-650 show interconnected network of nanocrystals with differently oriented GBs (**Fig. 1i,j** and **S4g,h**). For R-Cu-350, both large and small connected domains with randomly oriented GBs were observed (**Fig. S4c,d**). The lattice spacing of all R-Cu-T is ca. 0.21 nm, corresponding to the (111) facet of Cu. This is consistent with the XRD results (**Fig. S5a**). These results indicate the fabrication of (111) GBs in Cu and the density of Cu(111) GBs can be modulated by controlling the initial calcination temperature of Cu(OH)₂ precursor (R-Cu-650 ≈ R-Cu-500 > R-Cu-350 > R-Cu-200).

The electrochemical performance of all R-Cu-T was evaluated in CO₂-saturated 0.1 M KHCO₃ with a typical H-type cell. Compared to pure polished Cu foam (R-Cu foam), all R-Cu-T have effectively suppressed the hydrogen production with FE_{H2} decreasing from 83.1 % to 24.0 %, and greatly enhanced the selectivity for CO₂ reduction to CO (**Fig. 2a**). As the LSV curves in **Fig. S6** shown, all R-Cu-T displayed a larger current density and a lower onset potential in CO₂-saturated electrolyte than that in Ar-saturated electrolyte, suggesting that all the samples had better activity for eCO₂RR over the competing HER. **Fig. 2b**, **c** and **S7** show that the FE for CO increased with the increase of negative applied potentials till -1.0 V (vs. RHE) for all R-Cu-T, and the highest FE_{CO} of 52.3 % was achieved for R-Cu-650. This is contrary to the H₂ production. At -1.0 V (vs. RHE), the FE for CO production increased from 33.2 % to 50.5 % and that for H₂ production decreased from 41.9 % to 25.1 % with increasing original calcination temperature from 200 to 500 °C. Further increase in the calcination temperature to 650 °C gives negligible influence on the product distribution (**Fig. 2a**). To determine the composition of the produced syngas, the ratio of H₂ to CO for all R-Cu-T was compared at different applied potentials. As shown in **Fig. 2d**, a wide H₂/CO ratio from 0.46 to 2.78 was achieved. Importantly, R-Cu-500 and R-Cu-650 demonstrate low H₂/CO ratio of ca. 0.5 over a large potential range from -0.9 to -1.2 V (vs. RHE). Although the synthesized syngas presents different H₂/CO ratios, it is worth mentioning that the total FE for syngas of all R-Cu-T maintained at a range of 75–80 %.

Moreover, at the same potential, CO production rate increased with the increase of calcination temperature from 200 to 500 °C, and kept almost steady as the temperature further increasing to 650 °C (**Fig. 2e**). By comparison, the H₂ production rate decreased in the same experimental settings (**Fig. 2f**). This indicates that CO₂ reduction is boosted on

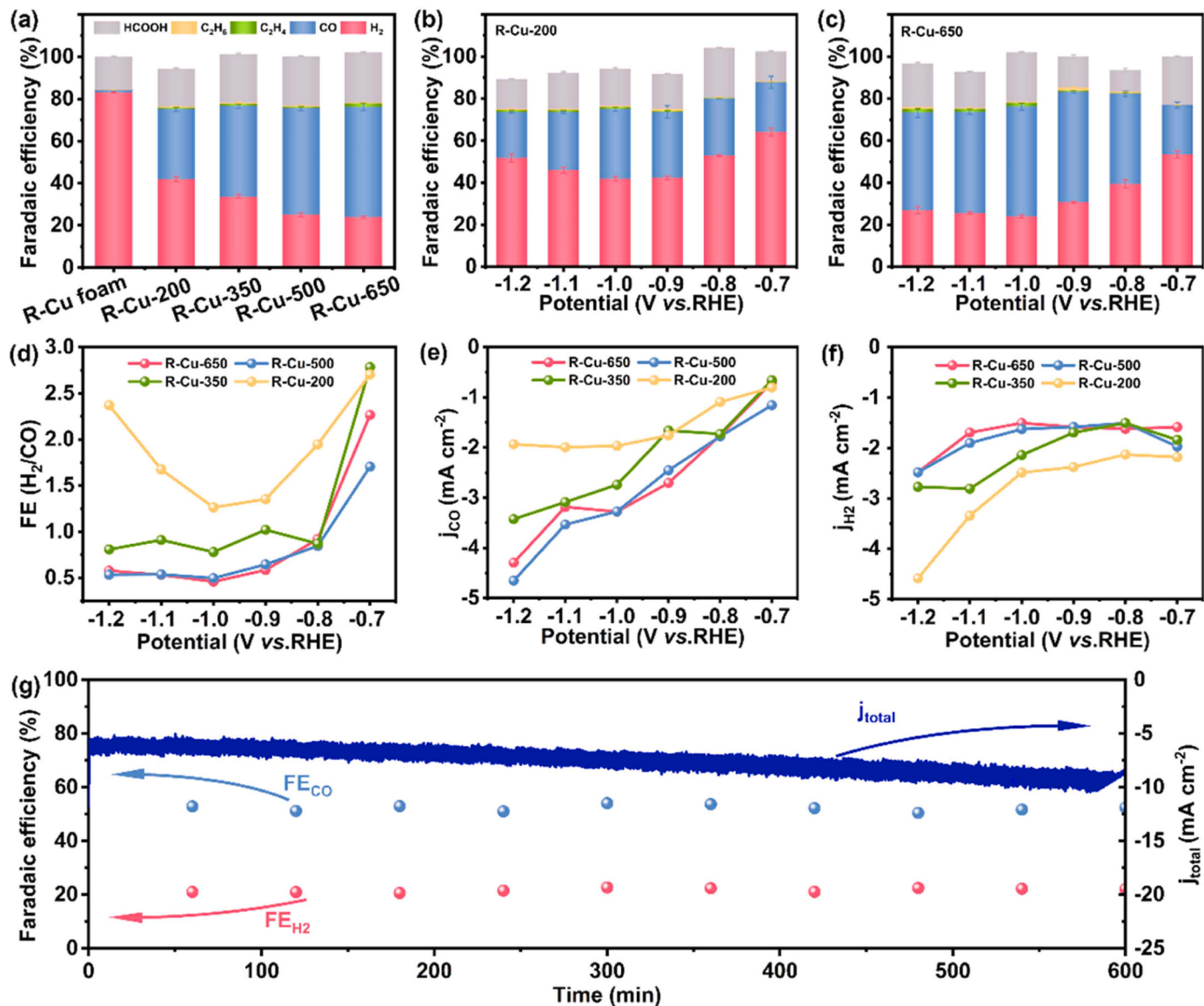


Fig. 2. eCO₂RR-to-syngas performance. (a) Comparation of FEs for different products on R-Cu foam and R-Cu-T at -1.0 V (vs. RHE); FEs for different products on (b) R-Cu-200 and (c) R-Cu-650 at applied potentials from -0.7 to -1.2 V (vs. RHE); (d) Ratio of H₂/CO on R-Cu-T at different potentials from -0.7 to -1.2 V (vs. RHE); Partial current density of (e) CO and (f) H₂ on R-Cu-T; (g) Long-term test of eCO₂RR-to-syngas on R-Cu-500 at -1.0 V (vs. RHE). The error bars represent the standard deviation of triplicate measurements.

R-Cu-500 and R-Cu-650. Particularly, the partial current density of syngas reached -7.13 mA/cm² at -1.2 V (vs. RHE) on R-Cu-500. Furthermore, the intrinsic activity of R-Cu-T was evaluated via normalizing the j_{CO} by ECSA, which was determined by measuring the double-layer capacitances (Fig. S8). The results demonstrate that ECSA-normalized activity for CO exhibits almost similar trend to that before normalization over different R-Cu-T (Fig. 2e and S8h). As expected, R-Cu-500 and R-Cu-650 show much higher intrinsic activity for CO than both R-Cu-200 and R-Cu-350.

It has been identified that GBs can control the product selectivity of eCO₂RR [39]. In this respect, the gradually enhanced CO production on R-Cu-200, R-Cu-350 and R-Cu-500/R-Cu-650 could be a good indication that Cu(111) GBs play a significant role in eCO₂RR-to-syngas. This is further verified by the experimental results of Cu(OH)₂ calcined at 800 °C. As shown in Fig. S9, a drastic agglomeration of Cu_xO polyhedron particles and collapse of 3D wormlike structure occurred to Cu_xO-800 and R-Cu-800, resulting in decreasing density of exposed Cu(111) GBs. Expectedly, the maximum FE for CO formation decreased from 52.3 % for R-Cu-650–45.8 % for R-Cu-800 at -1.0 V (vs. RHE).

In addition, take R-Cu-500 for instance, the stability for syngas formation at -1.0 V (vs. RHE) has been investigated (Fig. 2g). The total current density increases slightly over 10 h, and the FE for syngas is maintained over 75 % ($F_{CO} \approx 50\%$, $F_{H_2} \approx 25\%$) during stability test, indicating the high stability of prepared R-Cu-T for syngas formation. SEM and HRTEM images taken after eCO₂RR (R-Cu-500-used, Fig. S10a-d) show the well-maintained Cu morphological structure and density of Cu(111) GBs. XRD pattern measured after eCO₂RR shows Cu diffraction peaks identical to those before testing (Fig. S10e), indicating no obvious crystalline structure changes during the long-term test. In addition, high-resolution XPS of Cu 2p and Cu LM2 XAES spectra show that Cu⁺ species are prevalent on the surface of both R-Cu-500 and R-Cu-500-used with almost no difference (Fig. S10f,g) and the identification of Cu species in XPS and XAES spectra will be further discussed below. These results indicate the excellent stability for GBs density and chemical valance states of the as-prepared R-Cu-T catalysts. This is corresponding well with the stable eCO₂RR for syngas formation. It should be pointed out that the performance in terms of total current density essentially changes slightly from the initial ca. -6.0 mA cm⁻² to ca.

-10 mA cm^{-2} after 10 h and some structural modifications in the catalyst should occur. In order to shed light on this behavior, we calculated the ECSA of R-Cu-500-used. Expectedly, as shown in Fig. S8g, the C_{dl} increases from the initial $0.01603 \text{ mF cm}^{-2}$ to $0.02491 \text{ mF cm}^{-2}$ after 10 h, indicating a higher ECSA for R-Cu-500-used with respect to that before electrolysis experiment. This might be related to the slight increase of total current density. In addition, the stability tests of R-Cu-500 at more negative applied potential of -1.1 and -1.2 V (vs. RHE) were carried out. As shown in Fig. S11, the total current density and the FE for syngas are well-maintained over 6 h, further indicating the high stability of prepared R-Cu-T for syngas formation.

A comparation was also made between R-Cu-T and the reported electrocatalysts for syngas formation (Table S1). Comprehensively considering cost-efficiency, CO selectivity, H_2/CO ratios and stability, our work achieved relatively high FE_{CO} of 52.3 % and FE_{syngas} of $\sim 80\%$ with tunable H_2/CO ratios of 0.46–2.78 over R-Cu-T for 10 h, surpassing many reported catalysts [40,41]. Furthermore, the eCO₂RR performance of R-Cu-500 was measured using flow-cell configuration. As shown in Fig. S12, a FE of 74.7 % for syngas with FE_{CO} of 57.7 % and H_2/CO ratio of 0.29 was obtained at high current density of 50 mA cm^{-2} .

To ensure that the improved performance of eCO₂RR-to-syngas on R-Cu-T is indeed originated from the variety of Cu(111) GBs density, the effect of valence states of Cu should be excluded. As shown in Fig. 3a, crystalline structure evolution suggests that Cu(OH)₂ precursor was decomposed into CuO at a lower temperature of 200°C . When the temperature was increased to 350°C , Cu₂O appeared and the corresponding peaks intensified with the disappearance of CuO at further increased temperature of 500 and 650°C . The structural information and valance states of Cu_xO-T were further determined by Raman and XPS measurements (Fig. 3b-d). Raman peaks at around 281, 337 and 617 cm^{-1} in Cu_xO-200 and Cu_xO-350 correspond to the vibrations of Cu–O bonds in the CuO lattice [42]. The bands of CuO vanished in

Cu_xO-500 and Cu_xO-650, while Cu₂O dominated the catalyst surface, as evidenced by the fingerprint Raman bands at 141, 206, 412 and 630 cm^{-1} (Fig. 3b) [43–45]. High-resolution XPS results of Cu 2p in Fig. 3c show that both Cu²⁺ and Cu⁰/Cu⁺ are present on the surface of Cu_xO-200 and Cu_xO-350, while Cu⁰/Cu⁺ species dominate the surface of Cu_xO-500 and Cu_xO-650. To further differentiate the Cu⁺ species from Cu⁰, the Cu LM2 XAES spectra of Cu_xO-T are shown in Fig. 3d. A comparison with the Cu LM2 XAES spectra of Cu, Cu₂O and CuO (Fig. S13) gives a piece of evidence for the peak at 568.7 eV in Cu_xO-200 and Cu_xO-350 to be attributed to Cu²⁺ species, and the peak at 569.9 eV in Cu_xO-500 and Cu_xO-650 to belong to Cu⁺ species [46–48]. Therefore, we conclude that the majority of Cu in Cu_xO-200 exists as CuO, while that in Cu_xO-500 and Cu_xO-650 is in form of Cu₂O. Also, the Cu_xO-350 consists both of CuO and Cu₂O.

After pre-reduction at -1.2 V (vs. RHE) for 1.5 h, the diffraction peaks characteristic of CuO and Cu₂O disappeared (Fig. S5a), indicating the reduction of oxidized Cu phases or reconstruction of Cu_xO-T to small particles during pre-reduction. This is also confirmed by the Raman spectroscopy (Fig. S5b) due to the almost negligible vibration peaks of oxidized Cu in R-Cu-T. Whereas, the Cu 2p XPS and Cu LM2 XAES spectra show that Cu⁺ species are prevalent on the surface of these R-Cu-T with minor Cu⁰ (Fig. S5c,d). It has been proved that the conversion of CO₂ to CO occurs via the formation of *COOH intermediate, and Cu⁰ species are the active sites [49]. *COOH strongly adsorbs on Cu⁰ sites via its carbon or oxygen atom, which is most likely to make significant amounts of Cu⁰ to be oxidized into Cu⁺ species [50]. The adsorption of *COOH was further supported by the appearance of O=C=O signal in C 1s XPS spectra at $\sim 289.3 \text{ eV}$ over R-Cu-T (Fig. S14) [21,51]. Importantly, for the valance states of Cu species over all R-Cu-T, the difference is negligible, regardless of the initial states (Fig. 3 and S5). Therefore, these characterization data suggest that Cu_xO-T have all been reduced to metallic Cu, and the tunable performance of eCO₂RR-to-syngas over R-Cu-T is not mainly associated with specific oxidation states of Cu.

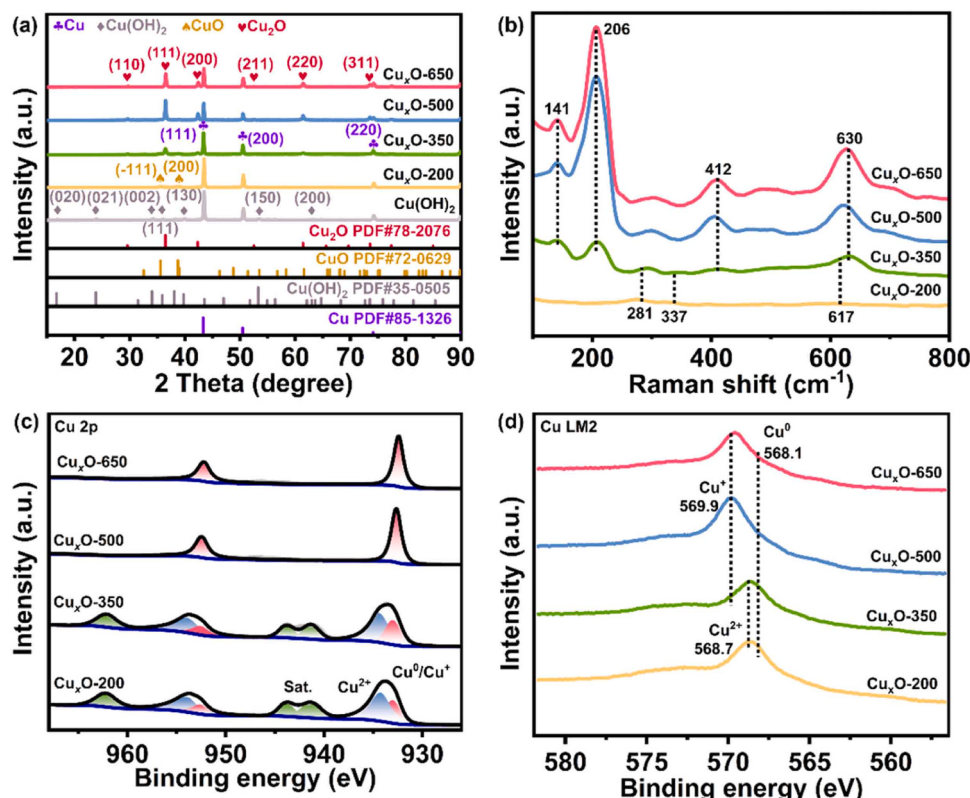


Fig. 3. (a) XRD images of Cu(OH)₂ precursor and calcined Cu_xO-T; (b) Raman spectra, (c) high-resolution Cu 2p XPS spectra, and (d) Cu LM2 XAES spectra of calcined Cu_xO-T.

To explore the impact of Cu(111) GBs on eCO₂RR-to-syngas over R-Cu-T and further illustrate the reaction mechanism, CO₂-TPD was conducted to study the adsorption of CO₂. As shown in Fig. 4a, compared to R-Cu-foam and R-Cu-200, R-Cu-650 had much higher CO₂ adsorption

capability, corresponding to the higher CO₂ reduction activity. Moreover, Tafel slopes of 107.5 mV/dec and 146.8 mV/dec were observed for R-Cu-500 and R-Cu-650, respectively. These Tafel slopes are close to a value of 118 mV/dec, indicating that the initial electron-transfer to

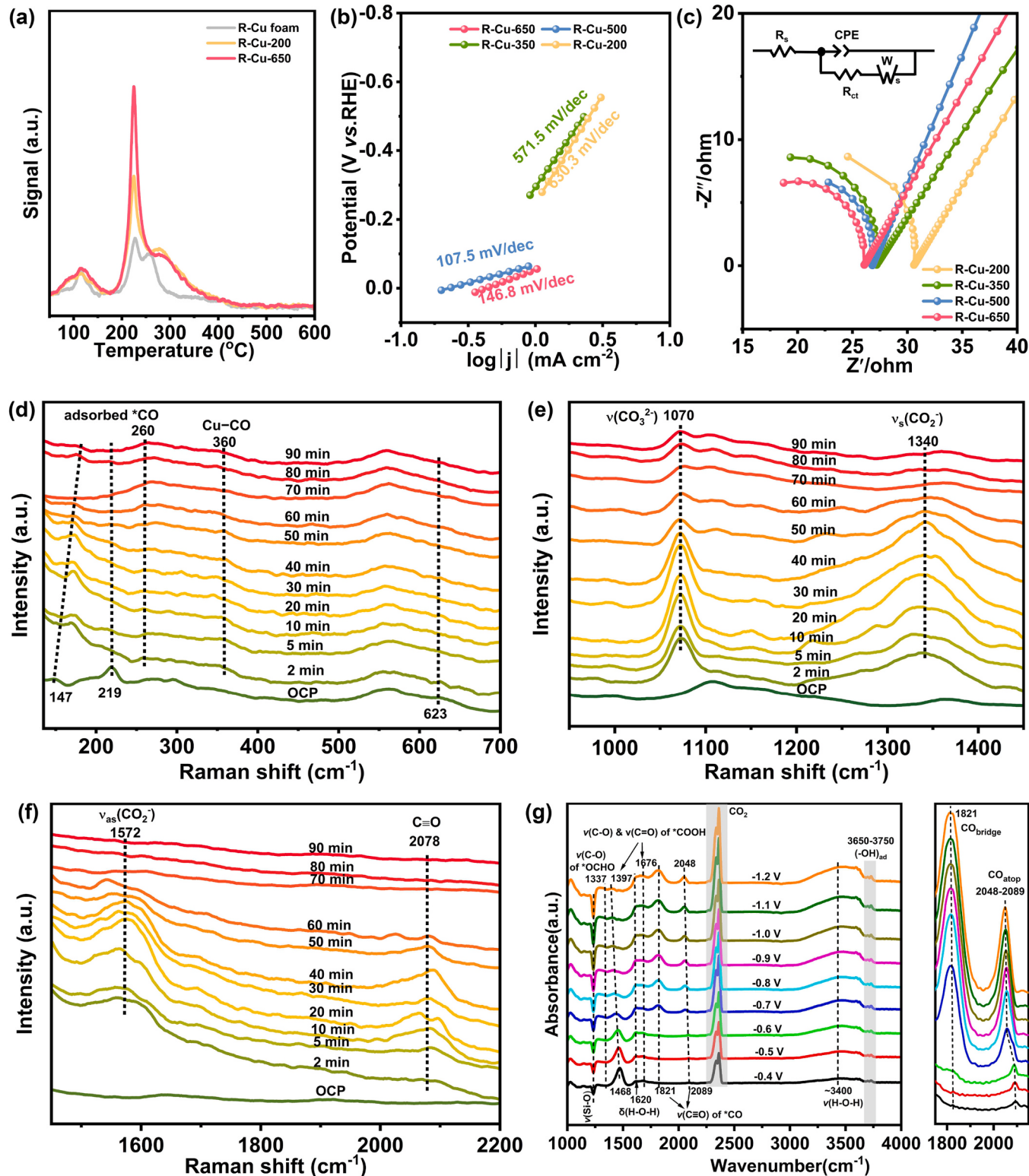


Fig. 4. (a) CO₂-TPD of R-Cu foam, R-Cu-200 and R-Cu-650; (b) Tafel plots of R-Cu-T; (c) EIS spectra of R-Cu-T and corresponding equivalent circuit used to fit the experimental impedance data. R_s , R_{ct} , CPE and W stand for solution resistance, charge transfer resistance, double-layer capacitance and Warburg-type impedance, respectively; (d-f) Time-resolved in situ Raman spectra of Cu_xO-650 for eCO₂RR at -1.2 V (vs. RHE); (g) Potential-dependent in situ ATR-SEIRAS spectra of Cu_xO-650 for eCO₂RR.

CO_2 to form an adsorbed $\text{CO}_2^{\bullet-}$ intermediate is the rate-determining step (RDS) [32,52]. While, much higher Tafel slopes of 571.5 mV/dec and 630.3 mV/dec obtained for R-Cu-350 and R-Cu-200 (Fig. 4b) suggested that electron-transfer step on the R-Cu-350 and R-Cu-200 was less facile than that on R-Cu-500 and R-Cu-650 [52]. Additionally, Tafel slopes for R-Cu-350 and R-Cu-200 are much higher than 118 mV/dec, implying that the mass transfer also plays a role in the reduction of CO_2 to CO for samples with low Cu(111) GBs density [47]. These results indicate that R-Cu-500 and R-Cu-650 exhibit intrinsically better activity and comparatively faster kinetics for CO_2 reduction, which are consistent with the superior e CO_2 RR-to-CO performance (Fig. 2a). Furthermore, the EIS of R-Cu-T and the corresponding equivalent circuit (Fig. 4c) were measured to study the interfacial charge transfer resistance between the electrolyte and electrode [53]. Compared with R-Cu-200 (14.82Ω) and R-Cu-350 (14.92Ω), R-Cu-500 (11.65Ω) and R-Cu-650 (12.23Ω) exhibited lower charge transfer resistance (R_{ct}), indicating that electron transfer to R-Cu-500 and R-Cu-650 is easier than to R-Cu-200 and R-Cu-350 during e CO_2 RR.

In addition, time-resolved in situ Raman spectra and potential-dependent in situ ATR-SEIRAS spectra were conducted to investigate the reaction mechanism of e CO_2 RR (Fig. 4d-g, S15,16 and Table S2). As shown in Fig. 4d and Fig. S16a,d,g, the vibration bands for surface CuO were observed at ~ 281 , ~ 342 and $\sim 617 \text{ cm}^{-1}$ on $\text{Cu}_x\text{O}-200/\text{Cu}_x\text{O}-350$, and vibration bands for Cu_2O were observed at ~ 147 , ~ 219 and $\sim 623 \text{ cm}^{-1}$ on $\text{Cu}_x\text{O}-350/\text{Cu}_x\text{O}-500/\text{Cu}_x\text{O}-650$ at OCP. At -1.2 V (vs. RHE), these peaks gradually disappeared with increasing reaction time, indicating CuO or Cu_2O species were reduced to metallic Cu, which was corresponding well with the XRD, XPS and ex situ Raman results before and after pre-reduction. These results further suggest the significant role of Cu^0 as the real active site. Concurrently, intense peaks of carbonate species at 1070 cm^{-1} , and symmetric and asymmetric C–O stretching vibrations of ${}^*\text{CO}_2^-$ intermediate at 1340 and 1572 cm^{-1} were detected on $\text{Cu}_x\text{O}-500$ and $\text{Cu}_x\text{O}-650$ (Fig. 4e,f and S16h,i), indicating the adsorption and initial conversion of CO_2 [54,55]. In contrast, these bands characteristic of CO_3^{2-} and ${}^*\text{CO}_2^-$ over $\text{Cu}_x\text{O}-200$ and $\text{Cu}_x\text{O}-350$ were relatively weak at the same time, which gives another piece of evidence that Cu(111) GBs enhance CO_2 adsorption and initial conversion. In addition, the gradually evolved peaks at 260 , 360 , and 2078 cm^{-1} are characteristic of the frustrated rotation of adsorbed ${}^*\text{CO}$, Cu–CO stretching vibration and intramolecular C≡O stretching vibration with top configuration (Fig. 4d,f) [56–59]. This reflects the interaction between ${}^*\text{CO}$ intermediate and Cu electrode surface. Expectedly, compared to $\text{Cu}_x\text{O}-200$ and $\text{Cu}_x\text{O}-350$ with low Cu(111) GBs density, intensities of these bands for adsorbed CO are much higher over $\text{Cu}_x\text{O}-500$ and $\text{Cu}_x\text{O}-650$ with abundant Cu(111) GBs. Interestingly, the intensity of band at 260 cm^{-1} is found to increase at the expense of peak at 2078 cm^{-1} over $\text{Cu}_x\text{O}-500$ and $\text{Cu}_x\text{O}-650$, which might be on account of the increased CO concentration [60]. This is in agreement with the experiment results that the selectivity of CO gradually increases during the pre-reduction (Fig. S3).

Fig. 4g, S15b and Table S2 show the in situ ATR-SEIRAS spectra of $\text{Cu}_x\text{O}-650$ recorded at the applied potentials from -0.4 to -1.2 V (vs. RHE), and the signal of $\text{Cu}_x\text{O}-650$ in CO_2 -saturated 0.1 M KHCO_3 at OCP was collected as a background. The peak intensity is expressed in absorbance, and the positive peak represents product generation. Expectedly, the bands characteristic of the C–O and C≡O stretching vibrations of ${}^*\text{COOH}$ species appeared at 1397 – 1468 cm^{-1} and 1676 cm^{-1} , which would be benefit for the production of CO [61–63]. Notably, the band for C–O stretching vibration of ${}^*\text{COOH}$ gradually decreased in intensity with the potential applying from -0.4 to -0.9 V (vs. RHE), and then kept steady with further increasing potential to -1.2 V (vs. RHE). Simultaneously, the bands attributed to C≡O stretching of linearly atop-bound CO and bridge-bound CO appeared at 2048 – 2089 cm^{-1} and 1821 cm^{-1} , respectively, and gradually increased in intensity with the consumption of ${}^*\text{COOH}$ [62,64–66]. The red shift of the bands for C–O stretching of ${}^*\text{COOH}$ and C≡O stretching of linearly

atop ${}^*\text{CO}$ at more negative potentials is caused by the Stark tuning effect [62,64]. In addition, a weak band attributed to symmetric C–O stretching vibrations of ${}^*\text{OCHO}$ was observed at $\sim 1337 \text{ cm}^{-1}$, which is the key intermediate for the formation of HCOOH, and the peak did not change with the applied potentials [67,68]. These results demonstrate that more CO is produced with the higher reduction energy input, whereas the formation of HCOOH is relatively stable with the applied potentials. This is also in line with the catalytic results (Fig. 2c). C 1 s XPS results of R-Cu-T give another piece of evidence for the formation of these intermediates (eg. ${}^*\text{CO}_2^-$, ${}^*\text{OCHO}$ and ${}^*\text{COOH}$), as the presence of an O=C=O signal for carboxyl group or carbonate ions at $\sim 289.3 \text{ eV}$ (Fig. S14). In addition, the multiple peaks in the range of 3650 – 3750 cm^{-1} are attributed to the surface hydroxyl from the dissociation of H_2O molecules, which supplies proton for generation of ${}^*\text{COOH}$ and ${}^*\text{OCHO}$ intermediates and production of H_2 [47,69].

DFT calculations were finally conducted to identify the role of Cu(111) GBs on e CO_2 RR and the corresponding reaction pathway of e CO_2 RR-to-syngas. Based on the HRTEM results and optimized adsorption configurations of intermediates on the model surface (Fig. 5a-e), reaction free energy diagrams for the evolution of CO_2 over Cu(111) facets and Cu(111) GBs were outlined to compare (Fig. 5f-h). Clearly, the element steps include CO_2 to ${}^*\text{COOH}$ and further to ${}^*\text{CO}$ and gaseous CO, and the overall reaction is determined by the protonation of CO_2 to ${}^*\text{COOH}$. Expectedly, its energy barrier on Cu(111) GBs (1.1 eV) is far lower than that on Cu(111) facets (2.6 eV), substantiating that the existence of abundant Cu(111) GBs is significant for lowering the formation energy barriers of ${}^*\text{COOH}$ and facilitating the formation of CO. In contrast, the formation of ${}^*\text{H}$ has a lower Gibbs free energy on the Cu(111) facet sites (2.9 eV) than that on the Cu(111) GBs (3.2 eV), implying that H_2 is more likely to form on Cu(111) facets. These results are in good agreement with the experimental observations that R-Cu-500 and R-Cu-650 with abundant Cu(111) GBs exhibit small H_2/CO ratios. Compared with the spontaneous step from ${}^*\text{COOH}$ to ${}^*\text{CO}$ on Cu(111) GBs (-0.3 eV), the much higher energy barrier of 1.5 eV for the generation of ${}^*\text{HCOOH}$ from ${}^*\text{OCHO}$ intermediate on Cu(111) GBs reveals that HCOOH formation is thermodynamically disadvantageous. This is in accordance with the catalytic results that R-Cu-500 and R-Cu-650 are more sensitive for the formation of CO than HCOOH. Based on these discussions, possible reaction pathways over R-Cu-T were proposed and illustrated in Fig. 5i and S17.

4. Conclusion

In summary, the fabrication of bare Cu catalysts with controllable density of (111) GBs through temperature-control annealing and pre-reduction was achieved. The as-prepared R-Cu-T exhibit a decent e CO_2 RR-to-syngas performance with tunable H_2/CO ratio of 0.46–2.78 and a high FE towards syngas of up to 80 %. Particularly, R-Cu-500/R-Cu-650 shows a stable H_2/CO ratio of ~ 0.5 over a wide potential window of -0.9 to -1.2 V (vs. RHE) and exhibits an excellent durability within 10 h with no obvious decays. It is demonstrated that 3D wormlike Cu with abundant (111) GBs promotes the adsorption of CO_2 , lowers the formation energy barriers of ${}^*\text{COOH}$ and ${}^*\text{CO}$ intermediates. In situ Raman, ATR-SEIRAS and DFT calculations tracked the evolution of catalysts in real time and revealed the thermodynamic favorable reaction pathway of e CO_2 RR-to-syngas. Therefore, this study highlights the broad prospects of GB modulating for designing high-performance electrocatalysts for e CO_2 RR.

CRediT authorship contribution statement

Shiying Li: Methodology, Formal analysis. **Zhikun Peng:** Methodology, Formal analysis. **Xueqi Liu:** Formal analysis. **Qun Xu:** Writing – review & editing, Supervision, Resources, Methodology, Funding acquisition, Formal analysis, Conceptualization. **Jiahao Wang:** Investigation, Formal analysis. **Hongpo Liu:** Writing – review & editing,

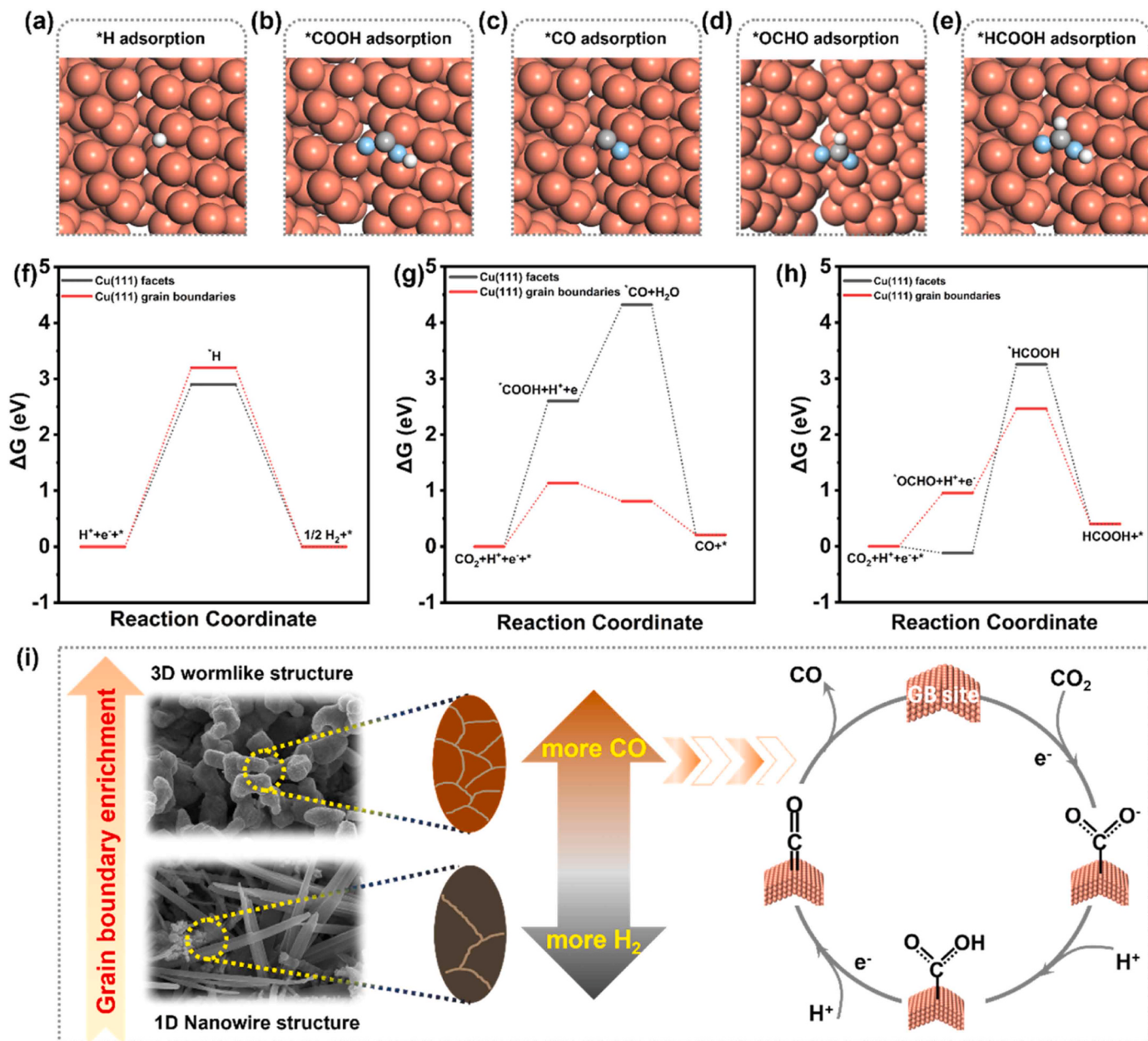


Fig. 5. Density functional theory results and possible reaction pathways. (a-e) DFT optimized geometries of (a) ${}^*\text{H}$, (b) ${}^*\text{COOH}$, (c) ${}^*\text{CO}$, (d) ${}^*\text{OCHO}$ and (e) ${}^*\text{HCOOH}$ on Cu(111) grain boundaries surface, H (white), C (grey), O (light blue); Free-energy diagrams of eCO₂RR to (f) H₂, (g) CO and (h) HCOOH; (i) Schematic of eCO₂RR over Cu with different density of (111) GBs and possible reaction pathway of CO₂ reduction to CO.

Supervision, Formal analysis. **Yaxi Li**: Data curation. **Huanhuan Yang**: Writing – review & editing, Supervision, Resources, Methodology, Funding acquisition, Formal analysis, Conceptualization. **Huiwen Tian**: Formal analysis. **Xia Bai**: Writing – original draft, Investigation, Formal analysis, Data curation, Conceptualization. **Jingmin Ge**: Writing – review & editing, Methodology, Formal analysis.

Declaration of Competing Interest

The authors declare that they have no known competing financial interests or personal relationships that could have appeared to influence the work reported in this paper.

Data availability

Data will be made available on request.

Acknowledgements

This work is supported by the Foundation of Henan Educational Committee (22A150024), the Natural Science Foundation of Henan Province (232300421364), the Natural Science Foundation of China (U2004208), the Innovative Team Program of Zhengzhou University, the Central Plains Science and Technology Innovation Leading Talent Project (234200510008), and the China Postdoctoral Science Foundation (2022TQ0351, GZC20232392). The density functional theory calculations were supported by National Supercomputing Center in Zhengzhou.

Appendix A. Supporting information

Supplementary data associated with this article can be found in the online version at doi:10.1016/j.apcatb.2024.124212.

References

- [1] M. Meinshausen, N. Meinshausen, W. Hare, S.C.B. Raper, K. Frieler, R. Knutti, D. J. Frame, M.R. Allen, Greenhouse-gas emission targets for limiting global warming to 2 °C, *Nature* 458 (2009) 1158–1162, <https://doi.org/10.1038/nature08017>.
- [2] S.A. Montzka, E.J. Dlugokencky, J.H. Butler, Non-CO₂ greenhouse gases and climate change, *Nature* 476 (2011) 43–50, <https://doi.org/10.1038/nature10322>.
- [3] P. Lu, D. Wu, L. Chen, H. Li, F. Wu, Air stability of solid-state sulfide batteries and electrolytes, *Electrochem. Energy Rev.* 5 (3) (2022), <https://doi.org/10.1007/s41918-022-00149-3>.
- [4] R. Purbia, S.Y. Choi, C.H. Woo, J. Jeon, C. Lim, D.K. Lee, J.Y. Choi, H.-S. Oh, J. M. Baik, Highly selective and low-overpotential electrocatalytic CO₂ reduction to ethanol by Cu-single atoms decorated N-doped carbon dots, *Appl. Catal. B-Environ.* 345 (2024) 123694, <https://doi.org/10.1016/j.apcatb.2024.123694>.
- [5] X. Wang, Q. Hu, G. Li, H. Yang, C. He, Recent advances and perspectives of electrochemical CO₂ reduction toward C₂₊ products on Cu-based catalysts, *Electrochem. Energy Rev.* 5 (2022) 28, <https://doi.org/10.1007/s41918-022-00171-5>.
- [6] Z. Chen, G. Zhang, H. Chen, J. Prakash, Y. Zheng, S. Sun, Multi-metallic catalysts for the electroreduction of carbon dioxide: recent advances and perspectives, *Renew. Sust. Energy Rev.* 155 (2022) 111922, <https://doi.org/10.1016/j.rser.2021.111922>.
- [7] T. Zhao, X. Zong, J. Liu, J. Chen, K. Xu, X. Wang, X. Chen, W. Yang, F. Liu, M. Yu, F. Cheng, Functionalizing Cu nanoparticles with fluoric polymer to enhance C₂₊ product selectivity in membrane CO₂ reduction, *Appl. Catal. B-Environ.* 340 (2024) 123281, <https://doi.org/10.1016/j.apcatb.2023.123281>.
- [8] S. Wang, Z. Qian, Q. Huang, Y. Tan, F. Lv, L. Zeng, C. Shang, K. Wang, G. Wang, Y. Mao, Y. Wang, Q. Zhang, L. Gu, S. Guo, Industrial-Level CO₂ electroreduction using solid-electrolyte devices enabled by high-loading nickel atomic site catalysts, *Adv. Energy Mater.* 12 (2022) 2201278, <https://doi.org/10.1002/aenm.202201278>.
- [9] D. Yang, Q. Zhu, X. Sun, C. Chen, W. Guo, G. Yang, B. Han, Electrosynthesis of a defective indium selenide with 3D structure on a substrate for tunable CO₂ electroreduction to syngas, *Angew. Chem. Int. Ed.* 59 (2020) 2354–2359, <https://doi.org/10.1002/anie.201914831>.
- [10] W. Ren, X. Tan, C. Jia, A. Krammer, Q. Sun, J. Qu, S.C. Smith, A. Schueler, X. Hu, C. Zhao, Electronic regulation of nickel single atoms by confined nickel nanoparticles for energy-efficient CO₂ electroreduction, *Angew. Chem. Int. Ed.* 61 (2022) e202203335, <https://doi.org/10.1002/anie.202203335>.
- [11] C. Jia, Y. Zhao, S. Song, Q. Sun, Q. Meyer, S. Liu, Y. Shen, C. Zhao, Highly ordered hierarchical porous single-atom Fe catalyst with promoted mass transfer for efficient electroreduction of CO₂, *Adv. Energy Mater.* 13 (2023) 2302007, <https://doi.org/10.1002/aenm.202302007>.
- [12] Z. Li, J. Liu, R. Shi, G.I.N. Waterhouse, X.-D. Wen, T. Zhang, Fe-based catalysts for the direct photohydrogenation of CO₂ to value-added hydrocarbons, *Adv. Energy Mater.* 12 (2022) 2200475, <https://doi.org/10.1002/aenm.202200475>.
- [13] S.P. Liu, M. Zhao, W. Gao, Q. Jiang, Mechanistic insights into the unique role of copper in CO₂ electroreduction reactions, *ChemSusChem* 10 (2017) 387–393, <https://doi.org/10.1002/cssc.201601144>.
- [14] H. Li, S. Cao, H. Sun, Y. Lu, Y. Zhang, X. Lu, J. Zeng, Z. Yan, CuNCN derived Cu-based/CNx catalysts for highly selective CO₂ electroreduction to hydrocarbons, *Appl. Catal. B-Environ.* 320 (2023) 121948, <https://doi.org/10.1016/j.apcatb.2022.121948>.
- [15] J. Zeng, M.R. Fiorentini, M. Fontana, M. Castellino, F. Risplendi, A. Sacco, G. Cicero, M.A. Farkhondehfal, F. Drago, C.F. Pirri, Novel insights into Sb-Cu catalysts for electrochemical reduction of CO₂, *Appl. Catal. B-Environ.* 306 (2022) 121089, <https://doi.org/10.1016/j.apcatb.2022.121089>.
- [16] H. He, D. Xia, X. Yu, J. Wu, Y. Wang, L. Wang, L. Wu, J. Huang, N. Zhao, L. Deng, Y.-N. Liu, Pd-SnO₂ interface enables synthesis of syngas with controllable H₂/CO ratios by electrocatalytic reduction of CO₂, *Appl. Catal. B-Environ.* 312 (2022) 121392, <https://doi.org/10.1016/j.apcatb.2022.121392>.
- [17] J.-F. Xie, J.-J. Chen, Y.-X. Huang, X. Zhang, W.-K. Wang, G.-X. Huang, H.-Q. Yu, Selective electrochemical CO₂ reduction on Cu-Pd heterostructure, *Appl. Catal. B-Environ.* 270 (2020) 118864, <https://doi.org/10.1016/j.apcatb.2020.118864>.
- [18] J. Kang, S. He, W. Zhou, Z. Shen, Y. Li, M. Chen, Q. Zhang, Y. Wang, Single-pass transformation of syngas into ethanol with high selectivity by triple tandem catalysis, *Nat. Commun.* 11 (2020) 827, <https://doi.org/10.1038/s41467-020-14672-8>.
- [19] L. Dai, Q. Qin, P. Wang, X. Zhao, C. Hu, P. Liu, R. Qin, M. Chen, D. Ou, C. Xu, S. Mo, B. Wu, G. Fu, P. Zhang, N. Zheng, Ultrastable atomic copper nanosheets for selective electrochemical reduction of carbon dioxide, *Sci. Adv.* 3 (2017) e1701069, <https://doi.org/10.1126/sciadv.1701069>.
- [20] P. Huang, S. Ci, G. Wang, J. Jia, J. Xu, Z. Wen, High-activity Cu nanowires electrocatalysts for CO₂ reduction, *J. CO₂ Util.* 20 (2017) 27–33, <https://doi.org/10.1016/j.jcou.2017.05.002>.
- [21] A. Niorettoni, R. Mazzaro, F. Liscio, A. Kovtun, L. Pasquini, S. Caramori, S. Berardi, Indium-modified copper nanocubes for syngas production by aqueous CO₂ electroreduction, *Dalton Trans.* 51 (2022) 10787–10798, <https://doi.org/10.1039/D2DT00779G>.
- [22] K. Chen, X. Zhang, T. Williams, L. Bourgeois, D.R. MacFarlane, Electrochemical reduction of CO₂ on core-shell Cu/Au nanostructure arrays for syngas production, *Electrochim. Acta* 239 (2017) 84–89, <https://doi.org/10.1016/j.electacta.2017.04.019>.
- [23] G. Glockler, Carbon–oxygen bond energies and bond distances, *J. Phys. Chem.* 62 (1958) 1049–1054, <https://doi.org/10.1021/j150567a006>.
- [24] H. Li, N. Zhang, S. Bai, L. Zhang, F. Lai, Y. Chen, X. Zhu, T. Liu, Strain-regulated Pd/Cu core/shell icosahedra for tunable syngas electrosynthesis from CO₂, *Chem. Mater.* 34 (2022) 7995–8003, <https://doi.org/10.1021/acs.chemmater.2c01917>.
- [25] Z. Chen, T. Wang, B. Liu, D. Cheng, C. Hu, G. Zhang, W. Zhu, H. Wang, Z.-J. Zhao, J. Gong, Grain-boundary-rich copper for efficient solar-driven electrochemical CO₂ reduction to ethylene and ethanol, *J. Am. Chem. Soc.* 142 (2020) 6878–6883, <https://doi.org/10.1021/jacs.0c00971>.
- [26] Q. Lei, H. Zhu, K. Song, N. Wei, L. Liu, D. Zhang, J. Yin, X. Dong, K. Yao, N. Wang, X. Li, B. Davaasuren, J. Wang, Y. Han, Investigating the origin of enhanced C₂₊ selectivity in oxide-/hydroxide-derived copper electrodes during CO₂ electroreduction, *J. Am. Chem. Soc.* 142 (2020) 4213–4222, <https://doi.org/10.1021/jacs.9b11790>.
- [27] X. Feng, K. Jiang, S. Fan, M.W. Kanan, Grain-boundary-dependent CO₂ electroreduction activity, *J. Am. Chem. Soc.* 137 (2015) 4606–4609, <https://doi.org/10.1021/ja5130513>.
- [28] X. Feng, K. Jiang, S. Fan, M.W. Kanan, A direct grain-boundary-activity correlation for CO electroreduction on Cu nanoparticles, *ACS Cent. Sci.* 2 (2016) 169–174, <https://doi.org/10.1021/acscentsci.6b00022>.
- [29] Z. Xu, T. Wu, Y. Cao, C. Chen, X. Zeng, P. Lin, W.-W. Zhao, Dynamic restructuring induced Cu nanoparticles with ideal nanostructure for selective multi-carbon compounds production via carbon dioxide electroreduction, *J. Catal.* 383 (2020) 42–50, <https://doi.org/10.1016/j.jcat.2020.01.002>.
- [30] C.W. Li, J. Ciston, M.W. Kanan, Electroreduction of carbon monoxide to liquid fuel on oxide-derived nanocrystalline copper, *Nature* 508 (2014) 504–507, <https://doi.org/10.1038/nature13249>.
- [31] A. Verdaguera-Casadevall, C.W. Li, T.P. Johansson, S.B. Scott, J.T. McKeown, M. Kumar, I.E.L. Stephens, M.W. Kanan, I. Chorkendorff, Probing the active surface sites for CO reduction on oxide-derived copper electrocatalysts, *J. Am. Chem. Soc.* 137 (2015) 9808–9811, <https://doi.org/10.1021/jacs.5b06227>.
- [32] Y. Chen, C.W. Li, M.W. Kanan, Aqueous CO₂ reduction at very low overpotential on oxide-derived Au nanoparticles, *J. Am. Chem. Soc.* 134 (2012) 19969–19972, <https://doi.org/10.1021/ja309317u>.
- [33] L. Cao, D. Raciti, C. Li, K.J.T. Livi, P.F. Rottmann, K.J. Hemker, T. Mueller, C. Wang, Mechanistic insights for low-overpotential electroreduction of CO₂ to CO on copper nanowires, *ACS Catal.* 7 (2017) 8578–8587, <https://doi.org/10.1021/acscatal.7b03107>.
- [34] C. Chen, X. Sun, L. Lu, D. Yang, J. Ma, Q. Zhu, Q. Qian, B. Han, Efficient electroreduction of CO₂ to C₂ products over B-doped oxide-derived copper, *Green Chem.* 20 (2018) 4579–4583, <https://doi.org/10.1039/C8GC02389A>.
- [35] W. Zhang, X. Wen, S. Yang, Y. Berta, Z.L. Wang, Single-crystalline scroll-type nanotube arrays of copper hydroxide synthesized at room temperature, *Adv. Mater.* 15 (2003) 822–825, <https://doi.org/10.1002/adma.200304840>.
- [36] X. Wang, Z. Jiang, P. Wang, Z. Chen, T. Sheng, Z. Wu, Y. Xiong, Ag⁺-doped InSe nanosheets for membrane electrode assembly electrolyzer toward large-current electroreduction of CO₂ to ethanol, *Angew. Chem. Int. Ed.* 62 (2023) e202313646, <https://doi.org/10.1002/anie.202313646>.
- [37] G. Li, Z.-C. An, J. Yang, J.-H. Zheng, L.-F. Ji, J.-M. Zhang, J.-Y. Ye, B.-W. Zhang, Y.-X. Jiang, S.-G. Sun, Revealing surface fine structure on PtAu catalysts by an in situ ATR-SEIRAS CO-probe method, *J. Mater. Chem. A* 11 (2023) 14043–14051, <https://pubs.rsc.org/en/content/articlelanding/2023/ta/d3ta01668d>.
- [38] A.A. Peterson, F. Abild-Pedersen, F. Studt, J. Rossmeisl, J.K. Norskov, How copper catalyzes the electroreduction of carbon dioxide into hydrocarbon fuels, *Energy Environ. Sci.* 3 (2010) 1311–1315, <https://doi.org/10.1039/C0EE00071J>.
- [39] S. Liu, J. Xiao, X.F. Lu, J. Wang, X. Wang, X.W. Lou, Efficient electrochemical reduction of CO₂ to HCOOH over Sub-2 nm SnO₂ quantum wires with exposed grain boundaries, *Angew. Chem. Int. Ed.* 58 (2019) 8499–8503, <https://doi.org/10.1002/anie.201903613>.
- [40] Z. Liang, L. Song, M. Sun, B. Huang, Y. Du, Tunable CO/H₂ ratios of electrochemical reduction of CO₂ through the Zn-Ln dual atomic catalysts, *Sci. Adv.* 7 (2021) eab14915, <https://doi.org/10.1126/sciadv.abl4915>.
- [41] J. Shen, L. Wang, X. He, S. Wang, J. Chen, J. Wang, H. Jin, Amorphization-activated copper indium core-shell nanoparticles for stable syngas production from electrochemical CO₂ reduction, *ChemSusChem* 15 (2022) e202201350, <https://doi.org/10.1002/cssc.202201350>.
- [42] F. Li, A. Thevenon, A. Rosas-Hernandez, Z. Wang, Y. Li, C.M. Gabardo, A. Ozden, D. Cao Thang, J. Li, Y. Wang, J.P. Edwards, Y. Xu, C. McCallum, L. Tao, Z.-Q. Liang, M. Luo, X. Wang, H. Li, C.P. O'Brien, C.-S. Tan, D.-H. Nam, R. Quintero-Bermudez, T.-T. Zhuang, Y.C. Li, Z. Han, R.D. Britt, D. Sinton, T. Agapie, J.C. Peters, E. H. Sargent, Molecular tuning of CO₂-to-ethylene conversion, *Nature* 577 (2020) 509–514, <https://doi.org/10.1038/s41586-019-1782-2>.
- [43] Q. Lei, L. Huang, J. Yin, B. Davaasuren, Y. Yuan, X. Dong, Z.-P. Wu, X. Wang, K. X. Yao, X. Lu, Y. Han, Structural evolution and strain generation of derived-Cu catalysts during CO₂ electroreduction, *Nat. Commun.* 13 (2022) 4857, <https://doi.org/10.1038/s41467-022-32601-9>.
- [44] S. Mu, H. Lu, Q. Wu, L. Li, R. Zhao, C. Long, C. Cui, Hydroxyl radicals dominate reoxidation of oxide-derived Cu in electrochemical CO₂ reduction, *Nat. Commun.* 13 (2022) 3694, <https://doi.org/10.1038/s41467-022-31498-8>.
- [45] P.-P. Yang, X.-L. Zhang, F.-Y. Gao, Y.-R. Zheng, Z.-Z. Niu, X. Yu, R. Liu, Z.-Z. Wu, S. Qin, L.-P. Chi, Y. Duan, T. Ma, X.-S. Zheng, J.-F. Zhu, H.-J. Wang, M.-R. Gao, S.-H. Yu, Protecting copper oxidation state via intermediate confinement for selective CO₂ electroreduction to C₂₊ fuels, *J. Am. Chem. Soc.* 142 (2020) 6400–6408, <https://doi.org/10.1021/jacs.0c01699>.
- [46] Z. Lyu, S. Zhu, M. Xie, Y. Zhang, Z. Chen, R. Chen, M. Tian, M. Chi, M. Shao, Y. Xia, Controlling the surface oxidation of Cu nanowires improves their catalytic selectivity and stability toward C₂₊ products in CO₂ reduction, *Angew. Chem. Int. Ed.* 60 (2021) 1909–1915, <https://doi.org/10.1002/anie.202011956>.

[47] L. Xue, C. Zhang, J. Wu, Q.-Y. Fan, Y. Liu, Y. Wu, J. Li, H. Zhang, F. Liu, S. Zeng, Unveiling the reaction pathway on Cu/CeO₂ catalyst for electrocatalytic CO₂ reduction to CH₄, *Appl. Catal. B-Environ.* 304 (2022) 120951, <https://doi.org/10.1016/j.apcatb.2021.120951>.

[48] T. Yan, P. Wang, Z.-H. Xu, W.-Y. Sun, Copper(II) frameworks with varied active site distribution for modulating selectivity of carbon dioxide electroreduction, *ACS Appl. Mater. Interfaces* 14 (2022) 13645–13652, <https://doi.org/10.1021/acsmami.2c00487>.

[49] X. Zhang, Y. Zhu, Z. Liu, F. Li, W. Zhou, Z. Dong, J. Fan, L. Liu, C. Du, Perforated nitrogen-rich graphene-like carbon nanolayers supported Cu-In catalyst for boosting CO₂ electroreduction to CO, *J. Energy Chem.* 75 (2022) 383–390, <https://doi.org/10.1016/j.jechem.2022.09.003>.

[50] H. Yang, Y. Chen, X. Cui, G. Wang, Y. Cen, T. Deng, W. Yan, J. Gao, S. Zhu, U. Olsbye, J. Wang, W. Fan, A highly stable copper-based catalyst for clarifying the catalytic roles of Cu⁰ and Cu⁺ species in methanol dehydrogenation, *Angew. Chem. Int. Ed.* 57 (2018) 1836–1840, <https://doi.org/10.1002/anie.201710605>.

[51] X. Xuan, J. Cheng, X. Yang, J. Zhou, Highly selective electrochemical reduction of CO₂ to CH₄ over vacancy–metal–nitrogen sites in an artificial photosynthetic cell, *ACS Sustain. Chem. Eng.* 8 (2020) 1679–1686, <https://doi.org/10.1021/acssuschemeng.9b07258>.

[52] H. Seong, M. Choi, S. Park, H.-w Kim, J. Kim, W. Kim, J.S. Yoo, D. Lee, Promoting CO₂-to-CO electroreduction via the active-site engineering of atomically precise silver nanoclusters, *ACS Energy Lett.* 7 (2022) 4177–4184, <https://doi.org/10.1021/acsenergylett.2c02018>.

[53] M. Wu, C. Zhu, K. Wang, G. Li, X. Dong, Y. Song, J. Xue, W. Chen, W. Wei, Y. Sun, Promotion of CO₂ electrochemical reduction via Cu nanodendrites, *ACS Appl. Mater. Interfaces* 12 (2020) 11562–11569, <https://doi.org/10.1021/acsami.9b21153>.

[54] G.-Y. Duan, X.-Q. Li, G.-R. Ding, L.-J. Han, B.-H. Xu, S.-J. Zhang, Highly efficient electrocatalytic CO₂ Reduction to C₂₊ products on a poly(ionic liquid)-based Cu⁰–Cu^I tandem catalyst, *Angew. Chem. Int. Ed.* 61 (2022) e202110657, <https://doi.org/10.1002/anie.202110657>.

[55] M. Xie, Y. Shen, W. Ma, D. Wei, B. Zhang, Z. Wang, Y. Wang, Q. Zhang, S. Xie, C. Wang, Y. Wang, Fast screening for copper-based bimetallic electrocatalysts: efficient electrocatalytic reduction of CO₂ to C₂₊ products on magnesium-modified copper, *Angew. Chem. Int. Ed.* 61 (2022) e202213423, <https://doi.org/10.1002/anie.202213423>.

[56] S. Yan, Z. Chen, Y. Chen, C. Peng, X. Ma, X. Lv, Z. Qiu, Y. Yang, Y. Yang, M. Kuang, X. Xu, G. Zheng, High-power CO₂-to-C₂ electroreduction on Ga-spaced, square-like Cu sites, *J. Am. Chem. Soc.* 145 (2023) 26374–26382, <https://doi.org/10.1021/jacs.3c10202>.

[57] D. Ren, J. Gao, L. Pan, Z. Wang, J. Luo, S.M. Zakeeruddin, A. Hagfeldt, M. Grätzel, Atomic layer deposition of ZnO on CuO enables selective and efficient electroreduction of carbon dioxide to liquid fuels, *Angew. Chem. Int. Ed.* 58 (2019) 15036–15040, <https://doi.org/10.1002/anie.201909610>.

[58] T.T.H. Hoang, S. Verma, S. Ma, T.T. Fister, J. Timoshenko, A.I. Frenkel, P.J. A. Kenis, A.A. Gewirth, Nanoporous copper–silver alloys by additive-controlled electrodeposition for the selective electroreduction of CO₂ to ethylene and ethanol, *J. Am. Chem. Soc.* 140 (2018) 5791–5797, <https://doi.org/10.1021/jacs.8b01868>.

[59] J. Gao, H. Zhang, X. Guo, J. Luo, S.M. Zakeeruddin, D. Ren, M. Grätzel, Selective C–C coupling in carbon dioxide electroreduction via efficient spillover of intermediates as supported by operando Raman spectroscopy, *J. Am. Chem. Soc.* 141 (2019) 18704–18714, <https://doi.org/10.1021/jacs.9b07415>.

[60] C. He, D. Duan, J. Low, Y. Bai, Y. Jiang, X. Wang, S. Chen, R. Long, L. Song, Y. Xiong, Cu₂–S derived copper nanoparticles: A platform for unraveling the role of surface reconstruction in efficient electrocatalytic CO₂-to-C₂H₄ conversion, *Nano Res.* 16 (2023) 4494–4498, <https://doi.org/10.1007/s12274-021-3532-7>.

[61] N.J. Firet, W.A. Smith, Probing the reaction mechanism of CO₂ electroreduction over Ag films via operando infrared spectroscopy, *ACS Catal.* 7 (2016) 606–612, <https://pubs.acs.org/doi/full/10.1021/acscatal.6b02382>.

[62] E.P. Delmo, Y. Wang, Y. Song, S. Zhu, H. Zhang, H. Xu, T. Li, J. Jang, Y. Kwon, Y. Wang, M. Shao, In situ infrared spectroscopic evidence of enhanced electrochemical CO₂ reduction and C–C coupling on oxide-derived copper, *J. Am. Chem. Soc.* 146 (2024) 1935–1945, <https://pubs.acs.org/doi/10.1021/jacs.3c08927>.

[63] Y. Katayama, F. Nattino, L. Giordano, J. Hwang, R.R. Rao, O. Andreussi, N. Marzari, Y. Shao-Horn, An in situ surface-enhanced infrared absorption spectroscopy study of electrochemical CO₂ reduction: selectivity dependence on surface C-bound and O-bound reaction intermediates, *J. Phys. Chem. C* 123 (2018) 5951–5963, <https://pubs.acs.org/doi/10.1021/acs.jpcc.8b09598>.

[64] Z.-Z. Wu, X.-L. Zhang, Z.-Z. Niu, F.-Y. Gao, P.-P. Yang, L.-P. Chi, L. Shi, W.-S. Wei, R. Liu, Z. Chen, S. Hu, X. Zheng, M.-R. Gao, Identification of Cu(100)/Cu(111) interfaces as superior active sites for CO dimerization during CO₂ electroreduction, *J. Am. Chem. Soc.* 144 (2022) 259–269, <https://doi.org/10.1021/jacs.1c09508>.

[65] S. Zhu, T. Li, W.-B. Cai, M. Shao, CO₂ electrochemical reduction as probed through infrared spectroscopy, *ACS Energy Lett.* 4 (2019) 682–689, <https://pubs.acs.org/doi/10.1021/acsenergylett.8b025>.

[66] C.M. Gunathunge, V.J. Ovalle, Y. Li, M.J. Janik, M.M. Waegele, Existence of an electrochemically inert CO population on Cu electrodes in alkaline pH, *ACS Catal.* 8 (2018) 7507–7516, <https://pubs.acs.org/doi/10.1021/acscatal.8b01552>.

[67] S. Liang, J. Xiao, T. Zhang, Y. Zheng, Q. Wang, B. Liu, Sulfur changes the electrochemical CO₂ reduction pathway over Cu electrocatalysts, *Angew. Chem. Int. Ed.* 62 (2023) e202310740, <https://doi.org/10.1002/anie.202310740>.

[68] K. Zhao, Y. Liu, X. Quan, S. Chen, H. Yu, CO₂ electroreduction at low overpotential on oxide-derived Cu/carbon fabricated from metal organic framework, *ACS Appl. Mater. Interfaces* 9 (2017) 5302–5311, <https://pubs.acs.org/doi/10.1021/acsmami.6b15402>.

[69] H. Noei, H. Qiu, Y. Wang, E. Löffler, C. Wöll, M. Muhler, The identification of hydroxyl groups on ZnO nanoparticles by infrared spectroscopy, *Phys. Chem. Chem. Phys.* 10 (2008) 7092–7097, <https://doi.org/10.1039/B811029H>.